LAWRENCE
LIVERMORE
NATIONAL
LABORATORY

Hilbert Space Inverse Wave Imaging in a Planar Multilayer Environment

Sean K. Lehman

November 2, 2004

Disclaimer

Hilbert Space Inverse Wave Imaging in a Planar Multilayer Environment

Sean K. Lehman

November 2, 2004

Abstract

Most diffraction tomography (DT) algorithms use a homogeneous Green function (GF) regardless of the medium being imaged. This choice is usually motivated by practical considerations: analytic inversions in standard geometries (Cartesian, spherical, etc.) are significantly simplified by the use of a homogeneous GF, estimating a non-homogeneous GF can be very difficult, as can incorporating a non-homogeneous GF into standard DT algorithms. Devaney has circumvented these issues by developing a purely numerical DT inversion algorithm [1] which is independent of measurement system geometry, number of frequencies used in the reconstruction, and GF. A planar multilayer GF has been developed for use in Devaney's "Hilbert space" algorithm and used to image non-invasively a flaw in a planar multilayer medium using data collected from an ultrasonic measurement system. The data were collected in a multistatic method with no beamforming: all focusing through the multilayer was performed mathematically "after-the-fact," that is after the data were collected.

UCRL-JRNL-207624

1 Introduction

Most diffraction tomography (DT) algorithms use a homogeneous Green function (GF) regardless of the medium being imaged. This choice is motivated by practical considerations: analytic inversions in "nice" (planar, circular, spherical, etc.) geometries are significantly simplified by the use of a homogeneous GF which has convenient decompositions in those coordinate systems, and, estimating a non-homogeneous GF and incorporating it into standard DT algorithms can be very difficult if not mathematically impossible. Devaney has circumvented these issues by developing a purely numerical DT inversion algorithm [1] which is independent of measurement system geometry, number of frequencies used in the reconstruction, and GF. It is based upon a projection operator interpretation of the forward scattering integral. The projection constitutes a Hilbert space mapping from a *continuous object space* to a *discrete measurement space*. The algorithm is described in detail in [1], and [2] where it was shown to be successful in reconstructing synthetic data from an annular outwardly-directed measurement system.

Here, we apply the Hilbert space algorithm to a planar multilayer domain with the goal of inverting a multistatic ultrasonic data set. To this end, we developed a scalar planar multilayer GF. Our GF solution is not new. Complete and detailed planar multilayer GF solutions have been previously derived for many applications [3, 4, 5, 6]. We do not, however, require the accuracy of these solutions since our reconstructions are limited by measurement noise and limited data. Additionally, we explicitly filter out evanescent field information since it is, for practical purposes, unusable at the propagation dimensions of our problem. We do require a model which accounts for the reverberation and multipath scattering within and between layers. We also require computational speed since our multilayer GF must be computed repeatedly over all combinations of transducers and frequencies.

The combination of the Hilbert space algorithm with the planar multilayer GF has successfully imaged a hole, the "flaw," in the copper layer of an aluminum/copper multilayer. The data were collected using a 5 MHz linear ultrasonic array in a multistatic method whereby each transmitter sequentially launched the primary field into the medium and the scattered field was measured at all receivers. No beamforming was performed during data collection: we accounted for the multilayer nature of the medium, mathematically through the multilayer GF, "after-the-fact," that is after the data were collected.

In most non-destructive evaluation (NDE) cases, prior knowledge of the internal structure of a part under evaluation is known via design or manufacturing specification. Thus, for NDE purposes, it is reasonable that the individual medium layer material properties and specifications are well known and understood. In this case, the inverse wave imaging is used to identify deviations from how the medium was assembled or built (the "as built" versus the "as designed" problem).

We review the derivation of the Hilbert space inverse wave algorithm in the next section. We summarize the development of our planar multilayer Green function in Section 3. The results are presented in Section 4 for simulated and experimental data sets on the aluminum/copper multilayer. Our conclusions are in Section 5.

2 Hilbert Space Inverse Wave Algorithm

The Hilbert space inverse wave (HSIW) algorithm [1, 2] interprets the forward scattering operator as a mapping from a continuous, real, object space to a discrete measurement space consisting of the discrete transceiver locations and, optionally, the discrete frequencies at which the measured data are collected. We summarize the HSIW algorithm here; details are presented in the references.

The forward scattering process is described by

$$\psi^{scat}(\mathbf{R}_m^r, \mathbf{R}_n^t, \omega) = k_0^2(\omega) \int d\mathbf{r}\, G_0(\mathbf{R}_m^r, \mathbf{r}, \omega)\, o(\mathbf{r})\, \psi(\mathbf{r}, \mathbf{R}_n^t \omega), \tag{1}$$

where

$\psi^{scat}(\mathbf{R}_m^r, \mathbf{R}_n^t \omega)$ is the *scattered* field measured at the mth receiver resulting from the nth source;

$\psi(\mathbf{r}, \mathbf{R}_n^t, \omega)$ is the *total* field resulting from the nth source;

$\mathbf{R}_m^r$ is the receiver location;

$\mathbf{R}_n^t$ is the source location;

ω is temporal frequency;

$k_0(\omega)$ is the background wavenumber defined as ω/v_0;

v_0 is the background velocity;

$G_0(\mathbf{R}_m^r, \mathbf{r}, \omega)$ is the homogeneous background Green function;

$o(\mathbf{r})$ is the object function to be imaged, defined as $(k^2(\mathbf{r})/k_0^2) - 1$, and;

$k(\mathbf{r})$ is the object function wavenumber.

The total field appearing under the integral of Eqn. 1 is the sum of the incident and scattered fields. In many instances it is possible to replace the total field by the incident field using the Born approximation. This permits the development of a linearized inversion of the integral. We assume the incident field is due to a point source located at $\mathbf{R}_n^t$:

$$\psi^{inc}(\mathbf{r}, \mathbf{R}_n^t, \omega) = P(\omega)\, G(\mathbf{r}, \mathbf{R}_n^t, \omega), \tag{2}$$

where $P(\omega)$ is the spectrum of the incident pulse. Substituting Eqn. 2 into Eqn. 1, we arrive at our forward, distorted Born approximation, scattering model:

$$\psi_B^{scat}(\mathbf{R}_m^r, \mathbf{R}_n^t, \omega_l) = P(\omega_l)\, k_0^2(\omega_l) \int d\mathbf{r}\, G_0(\mathbf{R}_m^r, \mathbf{r}, \omega_l)\, o(\mathbf{r})\, G(\mathbf{r}, \mathbf{R}_n^t, \omega_l), \tag{3}$$

where the B superscript indicates the approximation. As all the measured data will be discretized on a digital computer, we have explicitly discretized the frequencies at which the data are collected via ω_l where $l = 0, 1, \cdots, N_f - 1$ and N_f is the number of frequencies in the pulse band width.

The HSIW interprets Eqn. 3 as a mapping from a *continuous object space* to a *discrete measurement space*. The object space is the physical $\mathbf{r}$ space of the object function. The measurement space consists of the discrete transducer locations and temporal frequencies at which the scattered data are measured. The scattering operator projects the object onto the measurement space. To formulate explicitly Eqn. 3 as a projection operator, we define the forward propagation or projection kernel as

$$\Pi^*(\mathbf{r}) \equiv P(\omega_l)\, k_0^2(\omega_l)\, G_0(\mathbf{R}_m^r, \mathbf{r}, \omega_l)\, G(\mathbf{r}, \mathbf{R}_n^t, \omega_l), \tag{4}$$

where $\Pi(\mathbf{r})$ is a $J \equiv (N_{\text{src}} \times N_{\text{rcv}} \times N_f)$ element column vector, N_{src} is the number of sources, and N_{rcv} is the number of receivers. Mathematically, the projection is represented as an inner product between the object function and the kernel via,

$$D = \int d\mathbf{r} \, \Pi^*(\mathbf{r}) \, o(\mathbf{r}) \equiv \langle \Pi, o \rangle, \tag{5}$$

where D is a J element column vector of measured data values at each source, receiver, and frequency combination. Symbolically, we define the forward scattering operator, K, as

$$K[\cdot] \equiv \int d\mathbf{r} \, \Pi^*(\mathbf{r}) \, [\cdot]. \tag{6}$$

Using the mathematics of linear algebra, it is shown [1, 2] the inverse of Eqn. 6 which reconstructs the object function is

$$\hat{o}(\mathbf{r}) = \sum_{j=0}^{J-1} \frac{1}{\sigma_j^2} \, \Pi^T(\mathbf{r}) \, u_j u_j^\dagger D, \tag{7}$$

where the σ_j and u_j are the singular values and measurement space singular vectors of K, respectively. Explicitly, these are defined by the normal equations of the singular system:

$$K v_j(\mathbf{r}) = \sigma_j u_j, \tag{8}$$
$$K^\dagger u_j = \sigma_j v_j(\mathbf{r}), \tag{9}$$

where the u_j span the measured data space, and the $v_j(\mathbf{r})$ span the object space. The measurement system is inherently ill-conditioned due to the limited aperture of the measurement system which only measures part of the scattered field, and due to the loss of the evanescent field information. Thus, a subset of the singular values must be rejected: they carry no useful object information and must not be used in the reconstruction of Eqn. 7. A decision must be made on the number of singular values/vectors to use. We have chosen to use the *Best Rank N* approximation. We compute the ratio

$$R(N) = \frac{\displaystyle\sum_{j=0}^{N-1} \sigma_j^2}{\displaystyle\sum_{j=0}^{J-1} \sigma_j^2}, \tag{10}$$

where we assume the singular values are arranged from smallest to largest: $\sigma_0^2 \leq \sigma_1^2 \leq \cdots \leq \sigma_{J-1}^2$. Plotting $R(N)$, we graphically identify the point at which the function starts to rise rapidly. The index of the singular value at which this occurs, we label as J_0. With this value determined, our final reconstruction is

$$\hat{o}(\mathbf{r}) = \sum_{j=J_0}^{J-1} \frac{1}{\sigma_j^2} \, \Pi^T(\mathbf{r}) \, u_j u_j^\dagger D. \tag{11}$$

4

Our experience reconstructing both simulated and experimentally collected scattered field data have shown that this criterion works consistently well.

The HSIW algorithm versatility lies in its ability to form reconstructions using any geometrical transducer configuration and any number of frequencies. It requires only the Green functions of Eqn. 4. For the current case of interest, we take $G_0(\mathbf{r}, \mathbf{r}', \omega)$ to be the free space Green function,

$$G_0(\mathbf{r}, \mathbf{r}', \omega) = \begin{cases} \frac{i}{4} H_0^{(1)}(k_0(\omega)|\mathbf{r} - \mathbf{r}'|) & \text{2D,} \\ \\ \frac{1}{4\pi|\mathbf{r}-\mathbf{r}'|} e^{ik_0(\omega)|\mathbf{r}-\mathbf{r}'|} & \text{3D,} \end{cases} \tag{12}$$

which is used to propagate a field from a point within the medium to the receiver. For $G(\mathbf{r}, \mathbf{r}', \omega)$, we use a multilayer Green function which permits us to propagate a field from a transducer through the layers to a point within the medium. This enables us to focus "after-the-fact", that is, after the data have been collected without the use of beam forming, on targets within the multilayer structure. We develop our Green function in the next section.

3 Mathematical Statement of the Planar Multilayer Problem

Consider the planar multilayer geometry of Figure 1. Each layer is identified by its bottom boundary, z_l. The top most layer, layer 0, is defined by z_0. We assume the source is located on or above the top layer. The wavenumber associated with each layer is $k_l(\omega) \equiv v_l/\omega$ where v_l is the wave field propagation velocity and ω the temporal radial frequency. We wish to solve the Green function equation,

$$\left[\nabla^2 + k^2(z)\right] G(\mathbf{r}, \mathbf{r}', \omega) = -\delta(\mathbf{r} - \mathbf{r}'), \tag{13}$$

where the depth-dependent wavenumber, $k(z)$, is given by

$$k(z) = \begin{cases} k_0(\omega) & z \le z_0 \\ k_1(\omega) & z_0 < z \le z_1 \\ \qquad \vdots \\ k_{L-2}(\omega) & z_{L-3} < z \le z_{L-2} \\ k_{L-1}(\omega) & z > z_{L-2}, \end{cases} \tag{14}$$

the source location is $\mathbf{r}' \le z_0$ (that is, located on or above the top layer), and $G(\mathbf{r}, \mathbf{r}', \omega)$ is the planar multilayer Green function to be determined (for this section, the ω dependence is implicit). Following a method similar to Chapter 4 of [3], we separate the coordinate system into *planar* and *perpendicular* components: $\mathbf{r} \equiv (\mathbf{r}_\perp, z)$ and $\mathbf{r}' \equiv (\mathbf{r}'_\perp, z')$, and perform a planar Fourier transform (PFT) of Eqn. 13 along the planar, $\mathbf{r}_\perp$, coordinate using the transform pair,

$$\tilde{\psi}(\mathbf{k}_\perp, z) = \int d\mathbf{r}_\perp \, \psi(\mathbf{r}_\perp, z) \, e^{-i\mathbf{k}_\perp \cdot \mathbf{r}_\perp}, \tag{15}$$

$$\psi(\mathbf{r}_\perp, z) = \frac{1}{(2\pi)^n} \int d\mathbf{k}_\perp \, \tilde{\psi}(\mathbf{k}_\perp, z) \, e^{i\mathbf{k}_\perp \cdot \mathbf{r}_\perp}, \tag{16}$$

where n is the dimensionality of the problem, to achieve:

$$\left[\partial_z^2 + k^2(z) - |\mathbf{k}_\perp|^2\right] \tilde{G}(\mathbf{k}_\perp, z; \mathbf{r}'_\perp, z'; \omega) = -e^{-i\mathbf{k}_\perp \cdot \mathbf{r}'_\perp}\delta(z - z'). \tag{17}$$

Equation 17 is a one dimensional ordinary differential equation in z. We simplify the notation by defining

$$\gamma_l^2 \equiv k_l(z)^2 - \mathbf{k}_\perp^2, \tag{18}$$
$$w(\mathbf{r}'_\perp) \equiv e^{-i\mathbf{k}_\perp \cdot \mathbf{r}'_\perp}, \tag{19}$$

where the $z-$dependence in γ_n is implicit. With these definitions, the equation to be solved reads

$$\left[\partial_z^2 + \gamma_l^2\right] \tilde{G}(\mathbf{k}_\perp, z; \mathbf{r}'_\perp, z'; \omega) = w(\mathbf{r}'_\perp)\,\delta(z - z'). \tag{20}$$

In Sections 3.1 through 3.3, we develop the solution Eqn. 20 following a technique similar to that used by DiNapoli and Deavenport [4] although we use planar Cartesian rather than polar coordinates. The solution is derived analytically but computed numerically. A numerical inverse PFT is used compute $G(\mathbf{r}, \mathbf{r}', \omega)$ from $\tilde{G}(\mathbf{k}_\perp, z; \mathbf{r}'_\perp, z'; \omega)$. We develop the full solution by dividing the problem into three parts:

1. We solve the problem of two layers with a source in Section 3.1;

2. We develop the solution between two arbitrary source-free layers in Section 3.2;

3. We combine these two solutions in Section 3.3 to achieve the full multilayer solution.

3.1 Two Layers With A Source

The solution to Eqn. 20 in the top two layers is

$$\tilde{G}(\mathbf{k}_\perp, z; \mathbf{r}'_\perp, z'; \omega) = \begin{cases} A_<(\mathbf{k}_\perp, z')e^{-i\gamma_0 z} & z < z', \\\\ A_>(\mathbf{k}_\perp, z')e^{i\gamma_0 z} + R_0(\mathbf{k}_\perp)e^{-i\gamma_0 z} & z' < z \leq z_0 \\\\ T_1(\mathbf{k}_\perp)e^{i\gamma_1 z} + R_1(\mathbf{k}_\perp)e^{-i\gamma_1 z} & z > z_0, \end{cases} \tag{21}$$

where $A_<(\mathbf{k}_\perp, z')$ and $A_>(\mathbf{k}_\perp, z')$ are the point source field coefficients, $R_0(\mathbf{k}_\perp)$ is the layer 0 reflection coefficient, and, $T_1(\mathbf{k}_\perp)$ and $R_1(\mathbf{k}_\perp)$ are the layer 1 transmission and reflection coefficients, respectively. $R_1(\mathbf{k}_\perp)$ is included for completeness, were there *only* two layers, $R_1(\mathbf{k}_\perp) \equiv 0$. Equation 21 has five coefficients to be determined ($A_<(\mathbf{k}_\perp, z')$, $A_>(\mathbf{k}_\perp, z')$, $R_0(\mathbf{k}_\perp)$, $T_1(\mathbf{k}_\perp)$ and $R_1(\mathbf{k}_\perp)$). We impose field boundary conditions (BC) about the source location and z_0 interface to solve for the coefficients. The conditions are

- Continuity of $G(\mathbf{k}_\perp, z; \mathbf{r}'_\perp, z'; \omega)$ about the source location $z = z'$;

- Step discontinuity of $\partial_z G(\mathbf{k}_\perp, z; \mathbf{r}'_\perp, z'; \omega)$ about the source location $z = z'$;

- Continuity of $G(\mathbf{k}_\perp, z; \mathbf{r}'_\perp, z'; \omega)$ at the layer interface, $z = z_0$;

- Continuity of $\partial_z G(\mathbf{k}_\perp, z; \mathbf{r}'_\perp, z'; \omega)$ at the layer interface, $z = z_0$.

Applying the BC and simplifying, we arrive at the following matrix relationship between the transmission and reflection coefficients of each layer:

$$v_1 = U_1^{-1}(z_0) U_0(z_0) v_0, \tag{22}$$

where

$$U_0(z_0) \equiv \begin{bmatrix} \frac{i}{2\gamma_0} w(\mathbf{r}'_\perp) e^{i\gamma_0(z_0 - z')} & e^{-i\gamma_0 z_0} \\ \frac{i}{2} w(\mathbf{r}'_\perp) e^{i\gamma_0(z_0 - z')} & -\gamma_0 e^{-i\gamma_0 z_0} \end{bmatrix}, \tag{23}$$

$$v_0 \equiv \begin{bmatrix} 1 \\ R_0(\mathbf{k}_\perp) \end{bmatrix}, \tag{24}$$

$$U_l(z) \equiv \begin{bmatrix} e^{i\gamma_l z} & e^{-i\gamma_l z} \\ \gamma_l e^{i\gamma_l z} & -\gamma_l e^{-i\gamma_l z} \end{bmatrix}, \tag{25}$$

$$v_l \equiv \begin{bmatrix} T_l(\mathbf{k}_\perp) \\ R_l(\mathbf{k}_\perp) \end{bmatrix}. \tag{26}$$

Thus, given the boundary conditions, v_0, at the top layer (layer 0), we may solve for the layer 1 coefficients via Eqn. 22.

3.2 Solution Between Two Source-Free Layers

In a source-free region, Eqn. 20, reduces to

$$\left[\partial_z^2 + \gamma_l^2 \right] \tilde{G}(\mathbf{k}_\perp, z; \mathbf{r}'_\perp, z'; \omega) = 0. \tag{27}$$

The solution is

$$\tilde{G}(\mathbf{k}_\perp, z; \mathbf{r}'_\perp, z'; \omega) = \begin{cases} T_l(\mathbf{k}_\perp) e^{i\gamma_l z} + R_l(\mathbf{k}_\perp) e^{-i\gamma_l z} & z_{l-1} < z \leq z_l \\ T_{l+1}(\mathbf{k}_\perp) e^{i\gamma_{l+1} z} + R_{l+1}(\mathbf{k}_\perp) e^{-i\gamma_{l+1} z} & z_l < z \leq z_{l+1}. \end{cases} \tag{28}$$

Imposing continuity in the field and its derivative (there is no source within this region), we arrive at the relationship between the layer coefficients:

$$v_{l+1} = U_{l+1}^{-1}(z_l) U_l(z_l) v_l, \tag{29}$$

where we have used the definitions of Eqns 25 and 26. Eqn. 29 gives us a method for computing the transmission and reflection coefficients for the $(l+1)^{\text{th}}$ layer given those in the lth layer. In the next section we combine the results from this and the previous section to derive the full, multilayer Green function.

3.3 Full Multilayer Solution

Let there be L layers labeled from $[0, L-1]$ as shown in Figure 1. The full multilayer solution Green function which is a solution to Eqn. 20 is

$$\tilde{G}(\mathbf{k}_\perp, z; \mathbf{r}'_\perp, z'; \omega) = \begin{cases} A_<(\mathbf{k}_\perp, z')e^{-i\gamma_0 z} & z < z', \\[2ex] A_>(\mathbf{k}_\perp, z')e^{i\gamma_0 z} + R_0(\mathbf{k}_\perp)e^{-i\gamma_0 z} & z' < z \le z_0, \\[2ex] T_1(\mathbf{k}_\perp)e^{i\gamma_1 z} + R_1(\mathbf{k}_\perp)e^{-i\gamma_1 z} & z_0 < z \le z_1, \\[2ex] T_2(\mathbf{k}_\perp)e^{i\gamma_2 z} + R_2(\mathbf{k}_\perp)e^{-i\gamma_2 z} & z_1 < z \le z_2, \\[2ex] \vdots & \\[2ex] T_{L-1}(\mathbf{k}_\perp)e^{i\gamma_{L-1} z} + R_{L-1}(\mathbf{k}_\perp)e^{-i\gamma_{L-1} z} & z > z_{L-1}. \end{cases} \tag{30}$$

The coefficients, $A_<(\mathbf{k}_\perp, z')$, $A_>(\mathbf{k}_\perp, z')$, $\{R_l(\mathbf{k}_\perp)\}_{l=1}^{L-1}$, and $\{T_l(\mathbf{k}_\perp)\}_{l=0}^{L}$, are to be determined. $R_0(\mathbf{k}_\perp)$ and $T_{L-1}(\mathbf{k}_\perp)$ are set by the top and bottom layer boundary conditions (BC) imposed on Eqn. 20. Those BC are

$$v_0 = \begin{bmatrix} 1 \\ R_0(\mathbf{k}_\perp) \end{bmatrix} \quad \text{for the top layer,} \tag{31}$$

$$v_{L-1} = \begin{cases} \begin{bmatrix} T_{L-1}(\mathbf{k}_\perp) \\ 0 \end{bmatrix} & \text{for an infinite or non-reflecting bottom layer,} \\[4ex] \begin{bmatrix} T_{L-1}(\mathbf{k}_\perp) \\ T_{L-1}(\mathbf{k}_\perp) \end{bmatrix} & \text{for a perfectly reflecting bottom layer.} \end{cases} \tag{32}$$

The matching conditions for each layer are

$$\begin{array}{rcl} U_0(z_0)v_0 & = & U_1(z_0)v_1 \\ U_1(z_1)v_1 & = & U_2(z_1)v_2 \\ U_2(z_2)v_2 & = & U_3(z_2)v_3 \\ & \vdots & \\ U_{L-2}(z_{L-2})v_{L-2} & = & U_{L-1}(z_{L-2})v_{L-1} \end{array} \tag{33}$$

Eliminating all but the top and bottom coefficients of Eqns. 33, we find

$$v_0 = U_0^{-1}(z_0)U_1(z_0)U_1^{-1}(z_1)U_2(z_1)U_2^{-1}(z_2)U_3(z_2)\cdots U_{L-2}^{-1}(z_{L-2})U_{L-1}(z_{L-2})v_{L-1}. \tag{34}$$

8

We simplify the notation by defining

$$\mathcal{H} \equiv U_0^{-1}(z_0)U_1(z_0)U_1^{-1}(z_1)U_2(z_1)U_2^{-1}(z_2)U_3(z_2)\cdots U_{L-2}^{-1}(z_{L-2})U_{L-1}(z_{L-2}), \quad (35)$$

and expressing Eqn. 34 as

$$v_0 = \mathcal{H}v_{L-1}. \quad (36)$$

Solving Eqn. 36 for $R_0(\mathbf{k}_\perp)$ and T_{L-1} determines v_0 and v_{L-1}. The remaining coefficients are then calculated using Eqn. 29.

3.3.1 Solution For Infinite Bottom Layer

For an infinite bottom layer there is no reflection. Thus we set $R_{L-1}(\mathbf{k}_\perp) = 0$, reducing Eqn. 36 to

$$\underbrace{\begin{bmatrix} 1 \\ R_0(\mathbf{k}_\perp) \end{bmatrix}}_{v_0} = \underbrace{\begin{bmatrix} \mathcal{H}_{11} & \mathcal{H}_{12} \\ \mathcal{H}_{21} & \mathcal{H}_{22} \end{bmatrix}}_{\mathcal{H}} \underbrace{\begin{bmatrix} T_{L-1}(\mathbf{k}_\perp) \\ 0 \end{bmatrix}}_{v_{L-1}}, \quad (37)$$

which yields

$$T_{L-1}(\mathbf{k}_\perp) = \frac{1}{\mathcal{H}_{11}}, \quad (38)$$

$$R_0(\mathbf{k}_\perp) = \frac{\mathcal{H}_{21}}{\mathcal{H}_{11}} \quad (39)$$

as solution.

3.3.2 Solution For Perfectly Reflecting Bottom Layer

For a perfectly reflecting bottom layer, the reflection and transmission coefficients are identical. We set $R_{L-1}(\mathbf{k}_\perp) = T_{L-1}(\mathbf{k}_\perp)$, reducing Eqn. 36 to

$$\begin{bmatrix} 1 \\ R_0(\mathbf{k}_\perp) \end{bmatrix} = \begin{bmatrix} \mathcal{H}_{11} & \mathcal{H}_{12} \\ \mathcal{H}_{21} & \mathcal{H}_{22} \end{bmatrix} \begin{bmatrix} T_{L-1}(\mathbf{k}_\perp) \\ T_{L-1}(\mathbf{k}_\perp) \end{bmatrix}, \quad (40)$$

which yields

$$T_{L-1}(\mathbf{k}_\perp) = \frac{1}{\mathcal{H}_{11} + \mathcal{H}_{12}}, \quad (41)$$

$$R_0(\mathbf{k}_\perp) = \frac{\mathcal{H}_{21} + \mathcal{H}_{22}}{\mathcal{H}_{11} + \mathcal{H}_{12}} \quad (42)$$

as solution.

9

3.4 Practical Considerations for Evanescent Fields

In anticipation of working with multilayer parts whose layer thickness are many wavelengths, we explicitly filter out the evanescent field information prior to performing an inverse planar Fourier transform of Eqn. 30. Explicitly, we compute

$$G_{\mathrm{LP}}(\mathbf{r}, \mathbf{r}', \omega) \;=\; \mathcal{F}_{\mathrm{PFT}}^{-1} \left\{ \tilde{G}(\mathbf{k}_\perp, z; \mathbf{r}'_\perp, z'; \omega) h_l(\mathbf{k}_\perp) \right\}, \tag{43}$$

where $h_l(\mathbf{k}_\perp)$ is a depth-dependent Hanning window whose width is proportional to the $k_l(\omega)$ propagating frequency cut-off of the lth layer, $\mathcal{F}_{\mathrm{PFT}}^{-1}\{\cdot\}$ is the inverse planar Fourier transform of Eqn. 16, and the "LP" subscript on the Green function indicates that the Green function has been low-pass filtered. Referring to Eqn. 4, we set

$$G(\mathbf{r}, \mathbf{R}_n^t, \omega) \;=\; G_{\mathrm{LP}}(\mathbf{r}, \mathbf{R}_n^t, \omega).$$

This is motivated by the exponentially decaying nature of the evanescent field which, when back propagated in the presence of noise (measurement and numerical), results in instabilities. Additionally, as the field propagates from the source down through successive layers, we do not propagate fields that have been cut-off in higher layers to subsequent layers, even if they can support those spatial field frequencies. Explicitly, if

$$k_l(\omega) \;>\; k_{l-1}(\omega),$$

we only propagate frequencies up to $k_{l-1}(\omega)$ for all subsequent layers until a layer with a lower cut-off is encountered.

In Section 2, we reviewed the inversion algorithm. In Section 3, we summarized the derivation of the planar multilayer Green function to be used in the inversion algorithm. In the following sections, we apply our planar multilayer inversion algorithm to simulated and experimental data.

4 Experimental Setup & Full Wave Simulation

The experimental setup consisted of a 32 element 5 MHz ultrasonic array. The transducers had a 1 mm pitch and served as both sources and receivers. The measured data were fully multistatic in that each source successively launched the incident field into the medium and the scattered field was recorded at all receivers. No beamforming was performed during the data collection, nor did we account for the multilayer structure of the medium.

The part under evaluation was an aluminum block epoxy bonded onto a copper block. The aluminum layer was 13 mm thick; the copper layer was 9 mm thick. A "defect" in the form of a 1 mm radius hole was drilled into the middle of the copper layer. The experimental aluminum/copper multilayer setup is pictured in Figure 2.

In conjunction with the experiment, we performed a two-dimensional finite-difference time-domain (FDTD) simulation of the setup using E3D, an explicit 2D/3D elastic wave propagation

code developed at Lawrence Livermore National Laboratory [7, 8, 9, 10, 11, 12]. The code simulates full wave scattering and requires as inputs a longitudinal velocity distribution, a transverse velocity distribution, and a density distribution.

The FDTD simulation domain, shown in Figure 3, consisted of four layers: air, aluminum, copper, air. The physical parameters assigned to aluminum/copper layers, required by E3D, are shown in the graphic. An air-filled hole with a radius of 1 mm was inserted 4 mm below the aluminum/copper interface.

Both the simulation and experiment used a Gaussian windowed sine as incident pulse:

$$p(t) \quad = \quad \sin\left(\omega_0 t\right) e^{-t^2/(2\sigma^2)}, \tag{44}$$

where $\omega_0 \equiv 2\pi f_0$, $\sigma \equiv N_{\text{cyc}}/\omega_0$, and N_{cyc} is the number of cycles in the pulse. We used f_0=5 MHz and 5 cycles. The pulse spectrum magnitude is shown in Figure 4 for both the simulated and experimental data sets. The highlighted regions of the curves show the 58 discrete frequencies used in the reconstructions. As discussed in [2], the Hilbert space algorithm is computationally intensive and demanding upon computer storage. Thus, we were unable to use the full pass band of the pulse spectrum in our reconstructions. The Green function computed for the HSIW algorithm consisted of an air/aluminum/copper/air multilayer.

In processing both the experimental and simulated data, we discovered that shear (transverse) waves which are not modeled in the theory of Sections 2 and 3, corrupted the reconstructions when we used the entire 32 element aperture. This was caused by late arriving shear waves at receivers distant from the source. In order to filter out these slower moving shear waves, we processed the data using successive, over-lapping *sub-apertures* rather than the *full aperture*.

In full aperture processing (refer to Figure 5 (a)), the time series measured at *all* receivers are used for each transmitter. Scattered field time series seen at receivers farther removed from the transmitter, contained both the pressure (longitudinal) waves and later arriving shear waves. As the latter were not included in the models, they corrupted the reconstructions.

In sub-aperture processing, we formed sub-arrays consisting of a central transmitter/receiver surrounded by equal numbers of receivers as shown in Figure 5 (b). By sequentially indexing the sub-array over to the next transmitter/receiver, the entire data set was processed. In this manner, we succeeded in spatially reducing the shear wave corruption of the reconstruction algorithm. We wish to emphasize that the sub-aperture processing was performed after the data were collected.

The reconstructions are presented in Figures 6 and 7 for the simulated and experimental data sets, respectively. The top plot of Figure 6 (a) shows the Best Rank N curve of Eqn. 10 used for thresholding the singular values; the bottom shows the actual singular value distribution. Using the Best Rank N criterion, we determined the top 10% of the singular values should be used in the reconstruction in Figure 6 (b). The flaw is clearly visible and correctly located.

Figure 7 shows the results for the experimental data set. In this case, the top 13% of the singular values were used. The reconstruction of Figure 7 shows excellent localization and contrast of the flaw.

11

5 Conclusions

We developed a scalar planar multilayer Green function for use in the Hilbert space inverse wave tomographic algorithm and used the latter to image a flaw in an aluminum/copper multilayer. We demonstrated our ability to focus successfully through the multilayer medium "after-the-fact," that is after the data have been collected in a multistatic manner without beamforming or taking into account, during data collection, the multilayer nature of the part.

In most non-destructive evaluation (NDE) cases, prior knowledge of the integral structure of a part under evaluation is known via blueprints or other manufacturing specification. Thus, for NDE purposes, it is reasonable that the individual medium layer material properties and specifications are well known and understood. In this case, the inverse wave imaging is used to identify deviations from how the medium was assembled or built. This is the "as-built" versus the "as-designed" problem. This algorithm can also be used to determine and track the aging of parts. We hope to develop spherical and cylindrical multilayer Green functions for other NDE applications.

6 Acknowledgments

References

[1] A. J. Devaney and M. Dennison. Inverse scattering in inhomogeneous background media. *Inverse Problems*, **19**:855–870, 2003.

[2] S. K. Lehman and S. J. Norton. Radial reflection diffraction tomography. *The Journal of the Acoustical Society of America*, **116**(4), October 2004.

[3] Leonid M. Brekhovskikh. *Waves in Layered Media*. Academic Press, 1960. Translated from the Russian by David Lieberman.

[4] F. R. DiNapoli and R. L. Deavenport. Theoretical and numerical green's function field solution in a plane multilayer medium. *Journal of the Acoustical Society of America*, **67**(1):92–105, January 1980.

[5] D. L. Folds and C. D. Loggins. Transmission and reflection of ultrasonic waves in layered media. *Journal of the Acoustical Society of America*, **62**(5):1102–1109, November 1977.

[6] H. Schmidt and J. Glattetre. A fast field model for three-dimensional wave propagation in stratified environments based on the global matrix method. *Journal of the Acoustical Society of America*, **78**(6):2105–2114, December 1985.

[7] A. R. Levander. Fourth-order finite-difference p-sv seismograms. *Geophysics*, **53**:1425–1436, 1988.

[8] S. Larsen and J. Grieger. Elastic modeling initiative, part III: 3-D computational modeling. *Soc. Expl. Geophysi. Confer. Proc.*, **68**:1803–1806, 1998.

[9] S. Larsen, M. Antolik, and et. al. 3D simulations of scenario earthquakes in the San Francisco Bay area. *EOS Trans.*, **78**:487, 1997.

[10] R. Madariaga. Dynamics of an expanding circular fault. *Bulletin of the Seismological Society of America*, **66**(3):639–666, June 1976.

[11] J. Virieux. P-SV wave propagation in heterogeneous media: Velocity-stress finite-difference method. *Geophysics*, **51**(4):889–901, April 1986.

[12] Shawn Larsen and David Harris. Seismic wave propagation through a low-velocity nuclear rubble zone. Technical report, Lawrence Livermore National Laboratory, 7000 East Avenue, Livermore, CA 94550, 1993.
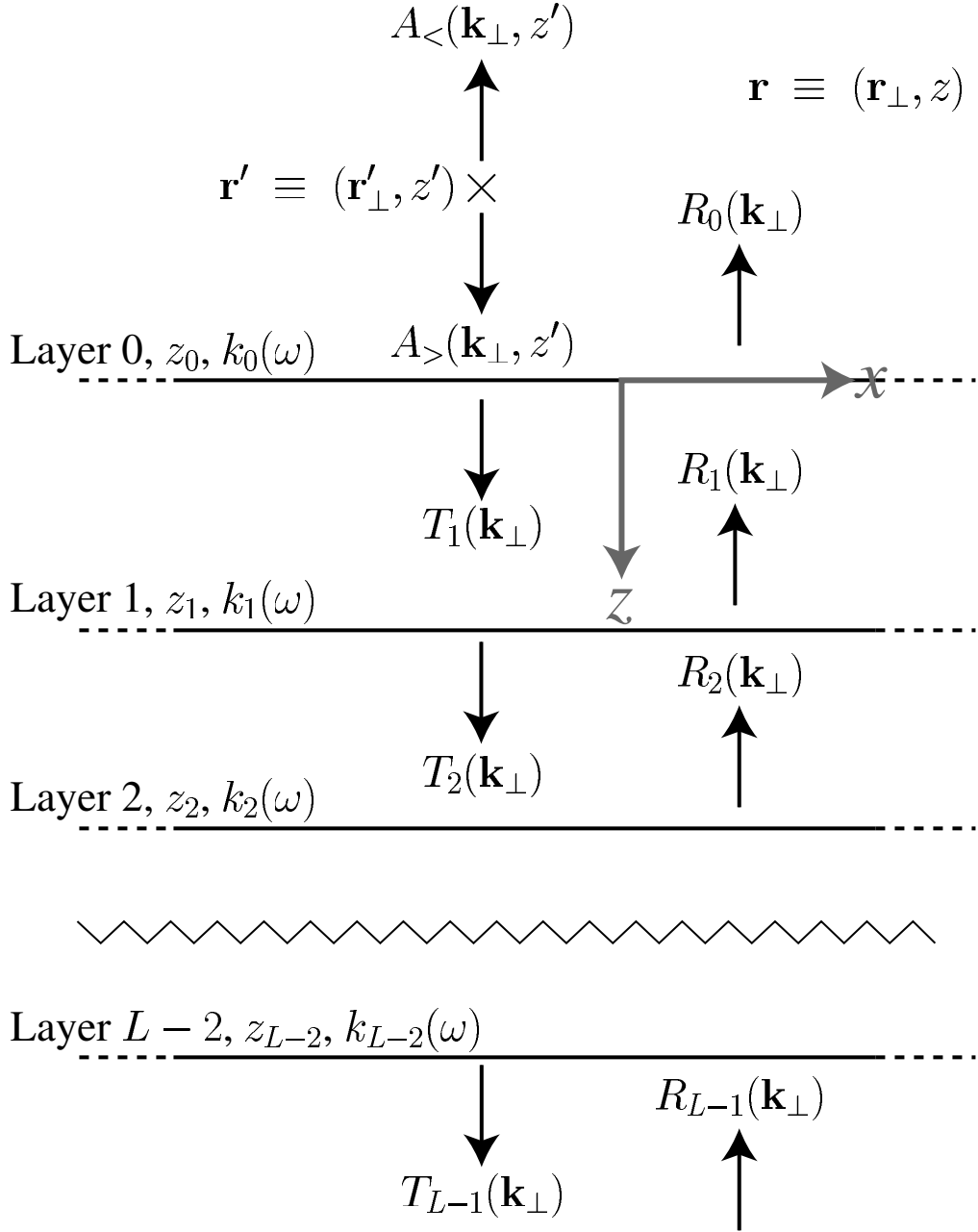
$$A_<(\mathbf{k}_\perp, z')$$

$$\mathbf{r} \equiv (\mathbf{r}_\perp, z)$$

$$\mathbf{r}' \equiv (\mathbf{r}'_\perp, z') \times$$

$$R_0(\mathbf{k}_\perp)$$

Layer 0, z_0, $k_0(\omega)$ $A_>(\mathbf{k}_\perp, z')$

x

$$T_1(\mathbf{k}_\perp)$$

$$R_1(\mathbf{k}_\perp)$$

z

Layer 1, z_1, $k_1(\omega)$

$$R_2(\mathbf{k}_\perp)$$

$$T_2(\mathbf{k}_\perp)$$

Layer 2, z_2, $k_2(\omega)$

Layer $L-2$, z_{L-2}, $k_{L-2}(\omega)$

$$R_{L-1}(\mathbf{k}_\perp)$$

$$T_{L-1}(\mathbf{k}_\perp)$$

Figure 1: *Multilayer geometry in the planar Fourier domain. There are $\{l\}_{l=0}^{L-1}$ layers. The source is located at $z' \leq z_0$.*
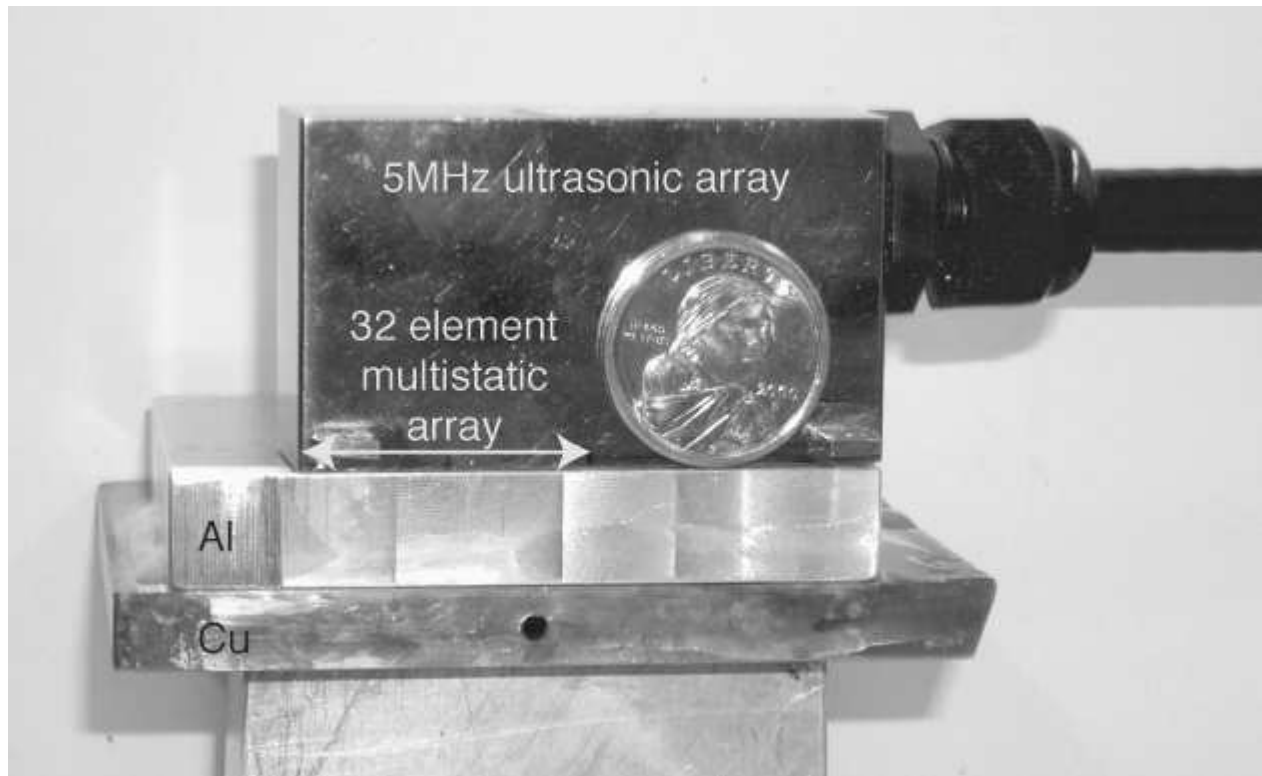
Figure 2: *Aluminum/Copper photograph. The aluminum bar below the copper layer is a support for the photograph and was not present during the data collection.*
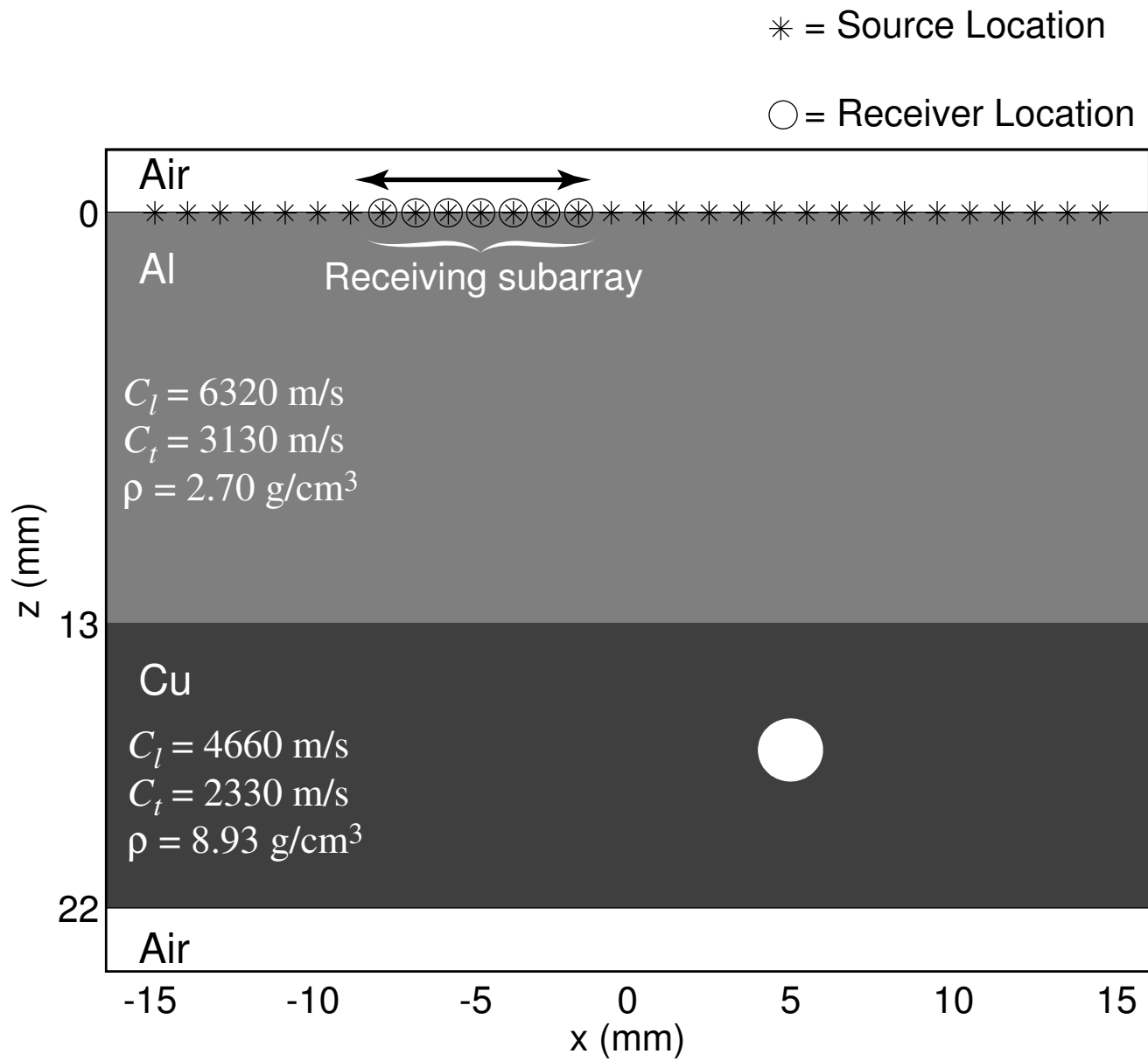
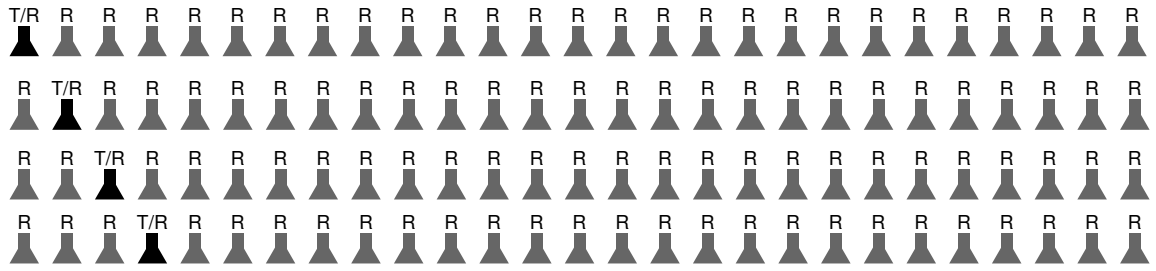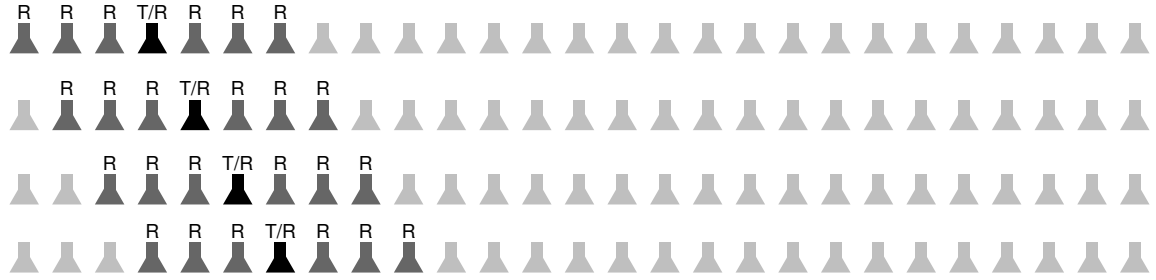Figure 3: *Air/Aluminum/Copper/Air multilayer simulation geometry.*
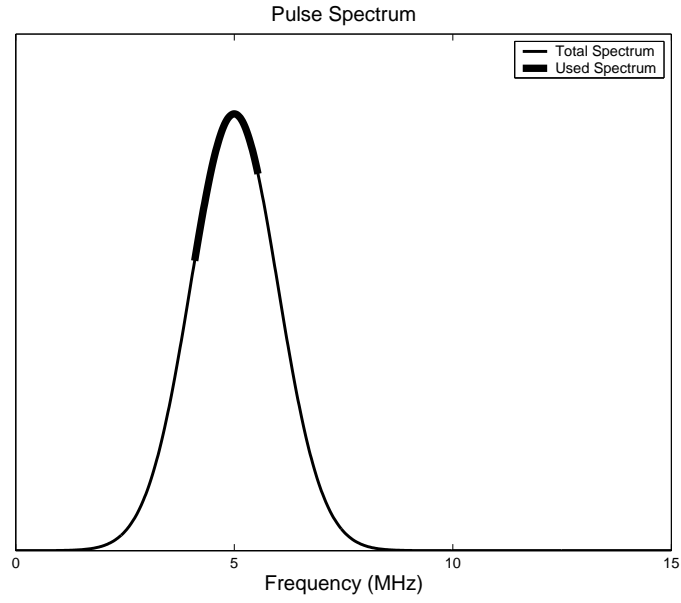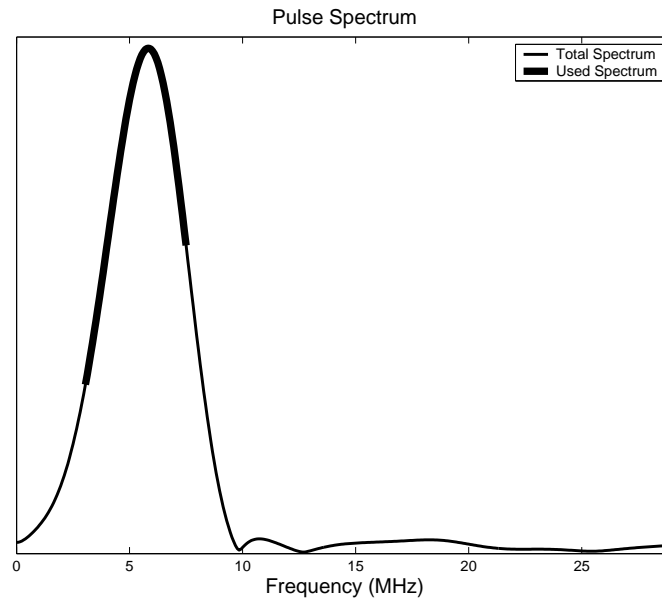
Figure 4: *Spectrum of 5 MHz, 5 cycle, Gaussian windowed sine spectrum magnitude used in (a) the FDTD simulation; and (b) the experiment. The highlighted parts of the curves show the 58 discrete frequencies used in the reconstructions.*
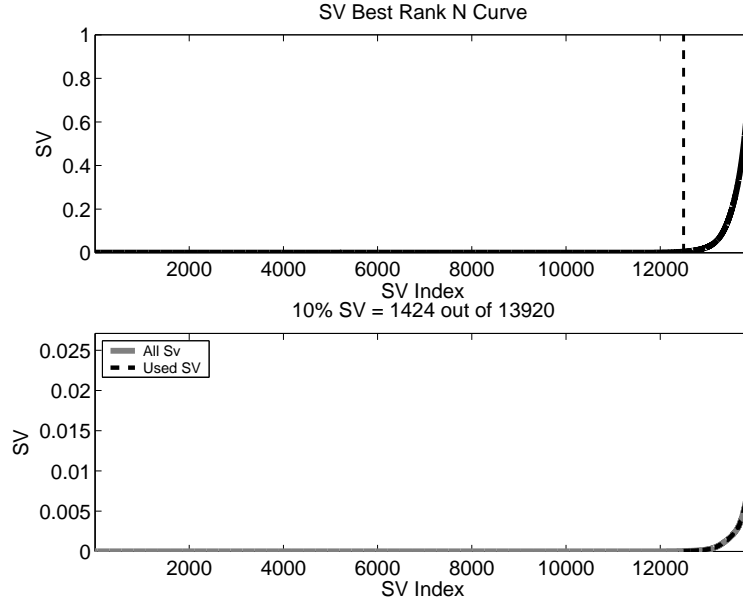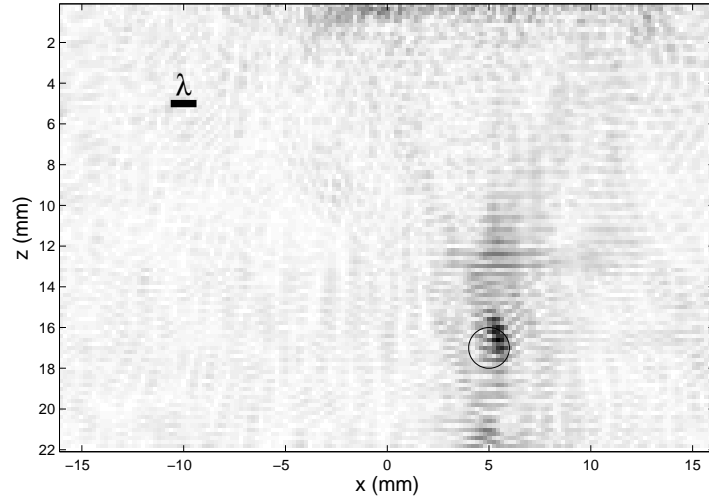
17

Figure 5: *Full aperture and sub-aperture processing. (a) In full aperture processing, the time series measured at all receivers are processed together. (b) In sub-aperture processing, the data from a shifting sub-array consisting of a transmitter/receiver surrounded by an equal number of receivers, are processed together.*

(a)

(b)

Figure 6: *Reconstruction of simulated data set. (a) The top plot shows the Best Rank N approximation of Eqn. 10. The dashed line shows the threshold below which none of the singular values were used in the reconstruction of Eqn. 11. The bottom plot shows the actual singular value distribution. (b) The reconstruction. The circle superposed on the image shows the true location of the flaw. The λ metric is the wavelength of the field in the top, aluminum, layer at $f_0 = 5$ MHz.*
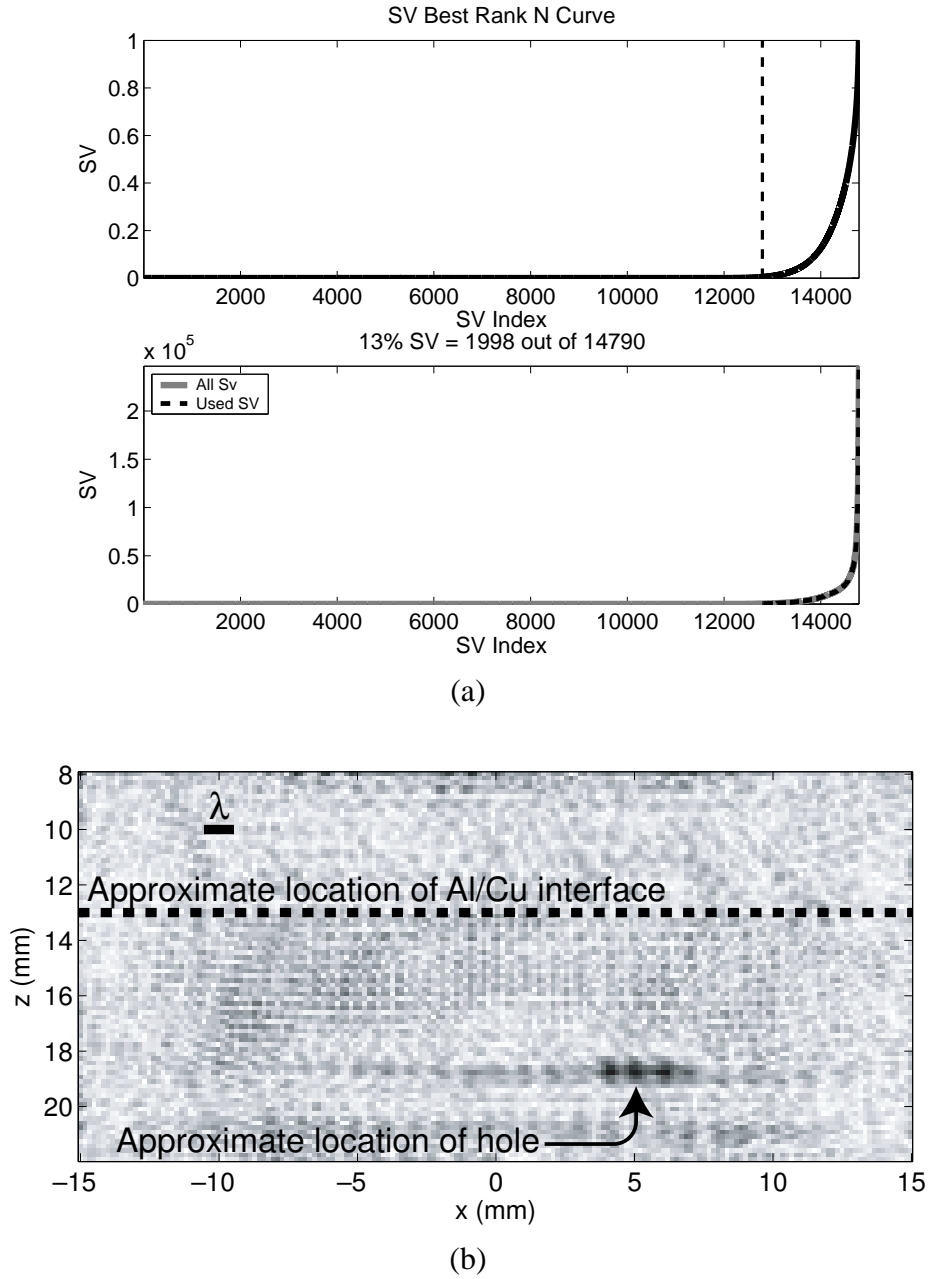
(a)

(b)

Figure 7: *Reconstruction of experimental data set. (a) The top plot shows the Best Rank N approximation of Eqn. 10. The dashed line shows the threshold below which none of the singular values were used in the reconstruction of Eqn. 11. The bottom plot shows the actual singular value distribution. (b) The reconstruction. The circle superposed on the image shows the approximate location of the flaw. The λ metric is the wavelength of the field in the top, aluminum, layer at $f_0 = 5$ MHz.*